Progress In Electromagnetics Research B, Vol. 34, 205–223, 2011

METAMATERIAL-BASED SENSOR DESIGN WORKING IN INFRARED FREQUENCY RANGE

L. La Spada*, F. Bilotti, and L. Vegni

Department of Applied Electronics, "Roma Tre" University, Via della Vasca Navale 84, Rome 00146, Italy

Abstract—In this paper, we propose the design of high sensitivity and selectivity metamaterial-based biosensors operating in the THz regime. The proposed sensors consist of planar array of resonant metallic structures, whose frequency response is modified through the variation of the surrounding dielectric environment. We consider different resonator geometries, such as the squared, circular, asymmetrical, and omega ones, and the analysis of the biosensors is conducted through proper equivalent quasi-static analytical circuit models. The metallic particles are assumed deposited on a glass substrate through proper titanium adhesion layers. Exploiting the proposed analytical model, which is verified through the comparison to full-wave numerical simulations, we study the biosensor resonance frequencies as a function of the geometric parameters of the individual inclusions. Finally, we optimize the structure in order to obtain high sensitivity and selectivity performances. The numerical results show that the proposed structures can be successfully applied as biosensors working in the THz region.

1. INTRODUCTION

The use of bio-electromagnetic sensors is of great interest in many application fields, such as medicine, microbiology, physics, environmental and personal safety. Sensors suitable for biomedical applications (e.g., to measure molecular concentrations, investigate the DNA, estimate the pH, etc.) are characterized by specific performance requirements [1]. Considering the wide range of applications involving detection and characterization of organic materials, a biosensor should be simultaneously highly sensitive and selective, possibly biocompatible, and immune to external

Received 3 June 2011, Accepted 10 September 2011, Scheduled 14 September 2011
* Corresponding author: Luigi La Spada (luigi.laspada@uniroma3.it).

disturbances, such as pressure or temperature changes. Photonics technologies allow to fabricate low-cost, compact, and high-performing biosensors. Among the others, optical sensors, in particular, are usually immune to electromagnetic interferences, compact and robust, compatible with fiber-optic networks, and compared to MEMS- (Micro-Electro-Mechanical-System) and MOEMS- (Micro-Opto-Electro-Mechanical-System) based sensors, exhibit a better response time and sensitivity [2, 3]. Such sensors are sensible to the variation of the refractive index of the surrounding environment, which is measured in different ways, depending on the specific architecture of the biosensor. However, the interaction between the sample and the optical signal is usually based on the variation of the refraction index phase, which is then converted to an amplitude variation through proper interferometric architectures. Among such architectures, the Mach-Zehnder one is widely used, due to its high sensitivity performances [4, 5]. From an operational point of view, such sensors make use of an integrated optical waveguide to confine the optical power, and usually detect the evanescent field diffused by the object. Though rather sensitive, interferometer configurations need quite large structures of the order of tens of mm. In order to overcome this limitation, photonic sensors based on micro-resonators have been recently proposed. They are much more compact in size (e.g., three orders of magnitude less) [6, 7] and exhibit a sensitivity which is comparable to the one of Mach-Zehnder-type sensors [8].

A relevant role is played by metamaterials as bio-electromagnetic sensors [9–11].

The aim of this paper is to design resonant-type metamaterial-based biosensors, operating in the THz regime. The advantages are:

- A reduction in the structure size, not losing sensitivity. In particular, a significant advantage of using a microresonator as a transducer is that the analyte volume, required for an accurate and reliable sensing, is reduced by several orders of magnitude. Such reduction allows to reach a very high sensitivity: the electromagnetic field is highly localized near the resonator, therefore the interaction between the field and the sample under test is restricted in a small sample area.
- Tuning the biosensor resonance to coincide with the spectral absorption characteristics of a selected organic group. This can be useful for the organic molecules detection, as many organic compounds contain bonds having molecular resonances in a particular spectral range.
- Increasing biosensing system performances: due to the small sample size, different arrays of resonators can be implemented on

a single chip to detect different biological samples simultaneously.

The general structure of the proposed biosensors consist of a planar array of metallic resonating inclusions deposited on a glass substrate and attached to it through proper adhesion layers. Since, according to the metamaterial concept, inclusion dimensions are much smaller than the operating wavelength, the electromagnetic behavior of the individual inclusion can be studied through a quasi-static approach leading to an equivalent circuit representation.

In Figure 1 the sensing system operation pattern is shown. The sensor SRR (without any material under test) has a specific resonant frequency. The sample is placed on top of the sensor. The presence of the sample changes the electromagnetic characteristics of the entire structure. Therefore the structure possess a resonant frequency different from the previous one in terms of width and position. The output signal is revealed in terms of reflection and transmission coefficient.

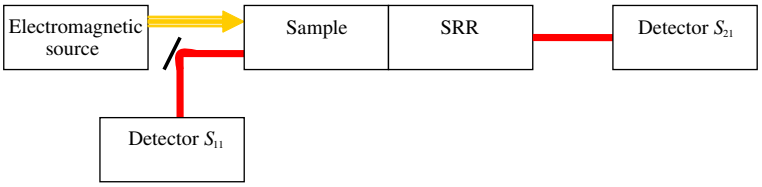

Figure 1. Block diagram of the metamaterial sensor.

In the paper, we first propose comprehensive equivalent circuit models of the inclusions, taking into account the presence of the glass substrate and the losses due to both the substrate and the metallic particles themselves. The results obtained through the proposed analytical models are then compared to the ones resulting from full-wave simulations performed through the finite-integration commercial code CST Studio Suite. Finally, the structures are optimized to get high selectivity and sensitivity performances. The proposed structures may find application in many fields, for instance in biomolecule detection, avoiding the employment of chemical markers (i.e., by using a label-free approach) and eliminating the artifacts caused by their use.

2. BRIEF DESCRIPTION OF THE QUASI-STATIC EQUIVALENT CIRCUIT MODEL

In this Section, we derive the quasi-static equivalent-circuit models for the analysis and design of different types of artificial magnetic

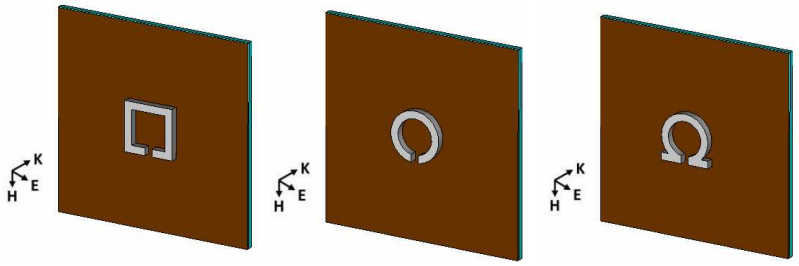

Figure 2. Geometrical sketch of the unit-cells of different biosensors: (a) squared split-ring, (b) circular split-ring, (c) omega particle.

resonators, such as the squared split-ring resonator, the loop split-ring resonator, and the omega resonator. The biosensors consist of planar arrays of such metallic inclusions. We assume first that the structure is excited by an impinging plane-wave having the electric and magnetic fields parallel and the propagation vector **k** perpendicular to the plane containing the biosensor, as depicted in Figure 2, where only the unit-cell is depicted. In this way, the resonators are excited by the electric field. The field, in fact, oscillates parallel to the gap and excites a conduction current in the resonators. As previously reported at microwave frequencies, the resonant behavior of the individual inclusions can be studied in terms of a proper equivalent LC resonant circuit [12, 13]. However, at higher frequencies (e.g., THz, infrared, and visible), the thickness of the metal can no longer be neglected and metals are not ideal conductors any more. At such frequencies, metals exhibit quite high losses and a dispersive behavior which can be represented in a given frequency range by the Drude model. Considering such additional effects, the equivalent circuit model of the individual inclusion is eventually the one reported in Figure 3, coming from [14].

3. EQUIVALENT CIRCUIT MODEL OF THE INDIVIDUAL INCLUSIONS

Considering the quasi-static equivalent circuit model reported in Figure 3, we evaluate in the following the lumped element parameters for three different types of resonators: squared split-ring, circular split-ring, and omega particle.

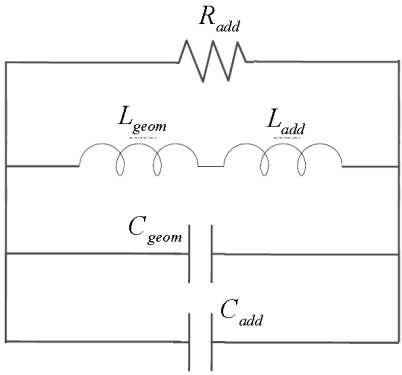

Figure 3. Quasi-static equivalent circuit model of a metallic particle in the infrared frequency range.

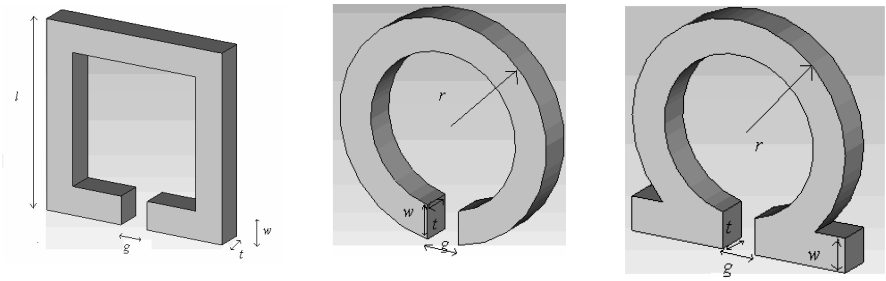

Figure 4. Relevant geometrical dimensions of the three resonators under analysis.

3.1. Squared Split-ring

3.1.1. Inductance Evaluation

Let's consider the geometrical sketch of the squared split-ring reported in Figure 4. The total inductance can be written as the sum of two contributions, the kinetic inductance (i.e., the additive term due to material non-idealities, according to [14]) and the geometric inductance, as follows:

$$L_{tot} = L_{geom}\,(l, w, t) + L_{add}\,(4l, w, t, \omega_p, y, \omega) \tag{1}$$

In parentheses we explicitly show the dependencies on the geometrical and electrical parameters characterizing the inclusion and the material.

The geometrical inductance of the squared split-ring can be easily obtained as the sum between the squared loop self-inductance and the

mutual inductances between the parallel bars of the squared particle. The self-inductance of the loop can be obtained from the inductance of a single three-dimensional bar reported in [15] as:

$$\begin{aligned} L(l,w,t) \;=\; & \frac{\mu_0}{4\pi} l \left\{ 2\ln[2l] - \frac{w^2}{3t^2}\ln[w] - \frac{t^2}{3w^2}\ln[t] \right. \\ & - \left(1 - \frac{t^2}{6w^2} - \frac{w^2}{6t^2}\right) \ln\left[w^2+t^2\right] - \frac{4}{3}\frac{w}{t}\tan^{-1}\left[\frac{t}{w}\right] \\ & \left. - \frac{4}{3}\frac{t}{w}\tan^{-1}\left[\frac{w}{t}\right] + \frac{13}{6} \right\} \end{aligned} \tag{2}$$

multiplied by 4. The mutual inductance between two parallel three-dimensional bars is given by [15]:

$$M(l,h) = \frac{\mu_0}{4\pi}\left\{ 2l\sinh^{-1}\left[\frac{l}{h}\right] + 2\left(h - \sqrt{h^2+l^2}\right)\right\} \tag{3}$$

Once the calculations are performed, the total geometrical inductance reads:

$$L_{geom} = 4L\left(l,w,t\right) - 4M\left(l,l-w\right) \tag{4}$$

For what concerns the kinetic additional inductance due to the role played at infrared and optical frequencies by the electron inertia, its formula is given by [14]:

$$L_{add}\left(l,w,t,\omega_p,\gamma,\omega\right) = \varepsilon_0 \frac{l}{wt}\frac{\omega^2+\gamma^2}{\omega^2\omega_p^2} \tag{5}$$

being l the length of the strip, w the strip width, t the thickness of the strip, ω the angular frequency [rad/s], ω_p and γ the plasma and damping frequency of the metallic material, respectively.

3.1.2. Capacitance Evaluation

Assuming ε_r the relative permittivity of the substrate, the total capacitance can be expressed as the sum of different parallel contributions:

$$\begin{aligned} C_{tot} \;=\; & C_g\left(w,t,g,\varepsilon_r\right) + C_f\left(w,g,\varepsilon_r\right) + C_s\left(w,t,g,r,\varepsilon_{\mathrm{sup}}\right) \\ & + C_{add}\left(4l,w,t,\varepsilon_r\right) \end{aligned} \tag{6}$$

where:

- C_g is the gap capacitance which can be expressed as a regular parallel plate contribution given by:

$$C_g\left(w,t,g,\varepsilon_r\right) = \varepsilon_0\varepsilon_r\frac{wt}{g} \tag{7}$$

- C_f is the fringing capacitance taking into account the contribution of the non-parallel electric field lines connecting the two gap plates. It has been obtained through a process of reversed engineering and proper fit of full-wave simulation data and reads [12]:

$$C_f\left(w,g,\varepsilon_r\right)=\varepsilon_0\varepsilon_r\frac{2w+\sqrt{2}g}{\pi}\cosh^{-1}\left[\frac{2w+g}{g}\right] \tag{8}$$

- C_s is the surface capacitance due to the charges on the metallic surfaces, as recently introduced in [16]. The corresponding expression reads [16]:

$$C_s=\left(w,t,g,r,\varepsilon_r\right)=2\varepsilon_0\varepsilon_r\frac{t+w}{\pi}\ln\left[\frac{4r}{g}\right]\quad r\cong\frac{2}{\pi}L \tag{9}$$

- C_{add} is the additional capacitance introduced in [14] taking into account the potential energy of the electrons stored in the metal. Its expression is given by:

$$C_{add}\left(l,w,t,\varepsilon_r\right)=\varepsilon_0\varepsilon_r\frac{tw}{l} \tag{10}$$

3.1.3. Resistance Evaluation

Since the inclusion is made by a non-ideal material and radiates energy, the total resistance is given by the contributions due to ohmic and radiation losses. However, in our configuration the radiation resistance of the particles plays a less important role, due to the effects of cancelation between the fields radiated by different elements of the planar array. Therefore, our interest here is mainly in the ohmic losses, taken into account by R_{add} [14]:

$$R_{add}\left(l,w,t,\omega_p,\gamma,\omega\right)=\frac{1}{\varepsilon_0}\frac{l}{wt}\frac{\omega^2+\gamma^2}{\omega_p^2\gamma} \tag{11}$$

It is worth noticing that losses degrade the quality factor of the resonator and some precautions should be taken at higher frequencies. On the other hand, the level of losses depends not only on the material used (ω_p and γ), but also on the shape of the particle (l, w, t), because these losses are due mainly to the scattering of electrons by the edges of the particle. In the end, thus, the choice of the optimal inclusion shape will strongly depend on the losses.

3.2. Circular Split-ring

The circuit parameters of the circular split-ring are obtained following the same procedure now outlined for the squared split-ring, starting

from the microwave geometrical capacitance and inductance already reported in the literature (see [17]) and adding the corresponding terms due to the non-idealities of metals at higher frequencies. For what concerns the latter terms, the geometrical lengths have been rounded considering the relation between the perimeter of a square and the circumference of the loop. The corresponding formulas are obtained straightforward and we do not report them here for the sake of brevity.

3.3. Omega Particle

As far as the resonant circuit of the omega particle is concerned, we have again applied the same procedure outlined for the split-ring structures, starting from the microwave geometrical inductance and capacitance reported in [18, 19]

3.4. Selection and Evaluation of the Substrate Impact

In order to take into account the effect of the substrate, starting from the assumptions given in [12], we have obtained the following closed-form formula for the effective permittivity of the substrate:

$$\varepsilon_{\text{sub}}\left(\varepsilon_r, h, w, s\right) = 1 + \frac{2}{\pi}(\varepsilon_r - 1)\sinh^{-1}\left[\frac{3}{2}\pi\sqrt{\frac{h}{(w+s)}}\right] \qquad (12)$$

Such formula has been derived through a process of reverse engineering with the following steps:

- choice of the substrate material (i.e., glass);
- study of the effect of the variation of the substrate thickness on the resonance frequency of the structure;
- evaluation of the corresponding values of the substrate effective permittivity;
- determination of the best-fit curve.

We list in the following some interesting considerations related to the proposed formula:

- when $0 \leq (h/w)$, $(h/s) \leq 1$ the substrate effective permittivity is a linear function of h/w and h/s;
- an increase in the thickness of the substrate corresponds to an increase in the effective permittivity;
- as expected, ε_{sub} tends to 1 when the substrate thickness h tends to 0.

In particular, for a glass substrate ($\varepsilon_g = 2.01$), by varying the substrate thickness between 10 and 100 nm, we obtain an agreement between full-wave numerical and analytical results above 95%.

3.5. Modeling of the Adhesion Layer

The deposition of metals on a glass substrate typically involves the use of an additional adhesion layer. TiO_2 is the most common thin film adhesive used to secure the metal to the dielectric substrate. In our design, we consider a TiO_2 5 nm thick adhesion layer on a 50 nm thick glass substrate is considered.

In order to model the effect of the adhesion layer, we adopt an effective medium approach. When two electrically thin material layers are stacked together, the total effective permittivity can be obtained by using the following equivalent expression:

$$\varepsilon_{eq} = \frac{\varepsilon_1 \varepsilon_2 (d_1 + d_2)}{\varepsilon_1 d_2 + \varepsilon_2 d_1} \tag{13}$$

In our case, being $\varepsilon_{TiO_2} = 7.84$ (TiO_2 relative permittivity) and $\varepsilon_g = 2.1$ (glass relative permittivity), one gets $\varepsilon_{eq} = 2.78$, which can be now put in the expression $\varepsilon_{\text{sub}}(\varepsilon_{eq}, h, w, s)$ to replace the regular relative permittivity of the substrate.

3.6. Comparison between Analytical and Numerical Model

Using the analytical circuit model depicted in Figure 2 and formulas (1)–(13), it is possible to analytically calculate analytically the resonant frequency of the individual inclusion. The resonant

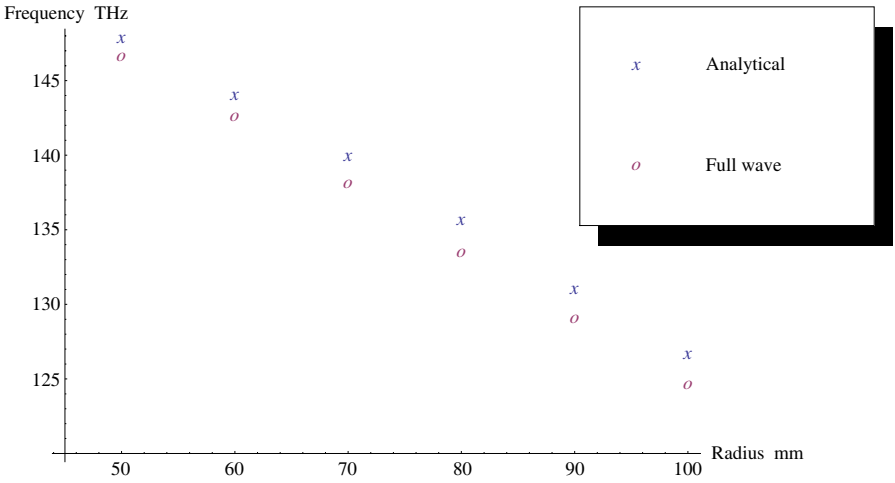

Figure 5. Error plot between Analytical and Numerical model (performed by full wave simulations) as a function of radius.

frequencies for different parameter configurations, obtained from full-wave simulations, are compared to the theoretical values, obtained from the proposed circuit model, as reported in Figure 5 and in Table 1.

To quantify the quality of the analytical circuit model over the desired frequency range, the following error was calculated and reported in Table 1

$$Error(\%) = \frac{f_{analytical} - f_{numerical\,CST}}{f_{numerical\,CST}}$$

As shown in Table 1 an agreement between full-wave numerical and analytical results was reached. As reported in [16], a good agreement between analytical and numerical model is reached when the error is less then 10%.

4. CHOICE OF THE INCLUSION: INFLUENCE OF GEOMETRICAL PARAMETERS

In order to design the inclusions of the planar array, we need to relate their resonant frequency to the geometrical parameters of the array (namely: gap length g, inclusion length l, strip width w, the spatial period Λ), to the metallic materials used for the inclusions, and to the thickness of the adhesion layer. The role of each of the aforementioned factors is briefly reviewed in Table 2.

Based on the results shown in Table 2, the position of the resonance peak depends on ω_p, g, l, w, t, $\varepsilon_{\mathrm{TiO_2}}$, while its bandwidth depends on γ, Λ and ε_g.

In view of the relations between the resonance frequency and the geometric/structural parameters we have optimized the electromagnetic response (finding the "optimal" values for r, l, g, w, Λ, and t) of the array to maximize selectivity and sensitivity. In Table 3,

Table 1. Error between analytical and numerical model (performed by full wave simulations) as a function of radius.

Radius (nm)	Resonant frequency (THz)		Error (%)
	Analytical model	Numerical model	
50	147.9	146.7	0.7
60	144.1	142.7	1
70	140	138.2	1.3
80	135.7	133.6	1.5
90	131.1	129.1	1.6
100	126.7	124.7	1.6

we anticipate the results of the optimization conducted, leaving the details to the following sections.

Table 2. The role of the geometrical parameters, metal properties, and adhesion layer thickness on the resonance frequency of the biosensor.

Parameters	**Changes on the resonance frequency (amplitude, position, bandwidth)**
Metal properties $\omega_p\,\gamma$	Increasing the plasma frequency ω_p determines a shift of the resonance frequency towards higher frequencies. Increasing the collision frequency γ results in an enlargement of the resonance peak.
Gap length g	Increasing the gap length, the resonance shifts towards higher frequencies.
Inclusion length l	Increasing the inclusion length leads to a reduction of the resonance frequency.
Strip width w	Increasing the strip width leads to a shift of the resonance frequency towards higher frequencies.
Spatial period Λ	The fundamental resonance frequency does not change when varying the period Λ. The resonance peak amplitude increases when the period the array decreases. The resonance peak broadens when the spatial period reduces.
Adhesion layer TiO_2	By increasing the thickness of the layer, the frequency peak shifts towards lower frequencies.

Table 3. Optimal geometrical parameters expressed in nm (r: radius of the circular split-ring and omega particle, l: length of the squared split-ring, g: gap length, w: strip width, t: metal thickness, Λ: spatial periodicity of the array). The refractive indices of glass and TiO_2 are kept constant at 1.45 and 2.8, respectively. Silver is modeled through a Drude model with $\omega_p = 2 \cdot \pi \cdot 2175 \cdot 10^{12}$ rad/s and $\gamma = 9 \cdot 10^{12}$. To date split ring are realized in different laboratories for further details see [20].

Parameters	r	l	g	w	t	Λ
Values	50	100	15	15	15	400

5. SELECTIVITY ANALYSIS

5.1. General Considerations

Selectivity is a measure of the performance of a sensor to respond only to the frequency it is tuned to. In order to get a high selective response, it is, thus, necessary that the sensor operates in a narrow frequency band. Exploiting the resonant circuits we have derived in the previous sections, it is possible to estimate the bandwidth of operation of the proposed sensors, as the inverse of the quality factors related to the resonances of the individual inclusions. In order to increase sensor selectivity, we need to increase the quality factor by:

- choosing a low-loss metal (decreasing γ, R increases accordingly);
- increasing the capacitance C of the inclusion (taking into account that this also reduces the resonant frequency);
- decreasing the inductance L (taking into account that the resonant frequency increases), by increasing the filling factor (i.e., increasing the amount of material in the unit-cell) and the strip width;
- reducing losses due to both the adhesion layer and the substrate (e.g., minimizing the thickness of the adhesion layer);
- moving the position of the gap around the inclusion to break the symmetry of the particles (asymmetric inclusions allow increasing the electromagnetic energy stored within the gap).

5.2. Analysis and Impact of the Substrate on the Quality Factor of the SRR

We have compared different geometries of inclusions keeping their occupied area and the following geometric/structural parameters —

Table 4. Quality factor values for different types of individual inclusions.

Squared split-ring	Asymmetric squared split-ring	U-shaped split-ring	Circular split-ring	Omega particle
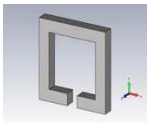	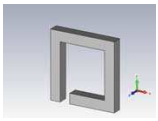	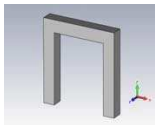	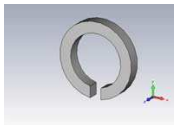	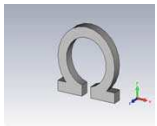
120	118	104	150	118

ω_p, r or l, g, w, t, Λ — constant. The expression used to relate the quality factor Q to the impedance bandwidth B is $Q = \omega_0/B$, where ω_0 is the resonant angular frequency. We have first considered the inclusions in free space and evaluated the corresponding quality factor, as reported in Table 4.

The effect of the glass substrate and of the adhesion layer is to reduce the quality factor, due to the additional volume of the device and the related losses. The corresponding values of the quality factor for the different inclusion shapes are reported in Table 5.

In summary, we have found out that as far as selectivity is the only parameter of interest, the circular split-ring is the best individual inclusion, while the squared split-ring, the asymmetric split-

Table 5. Quality factor values for different individual inclusions considering the effect of both substrate and adhesion layer.

Squared split-ring	Asymmetric squared split-ring	U-shaped split-ring	Circular split-ring	Omega particle
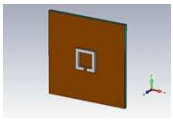	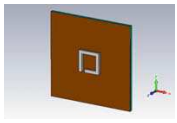	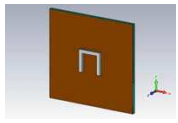	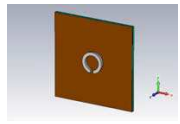	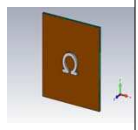
90	90	70	105	90

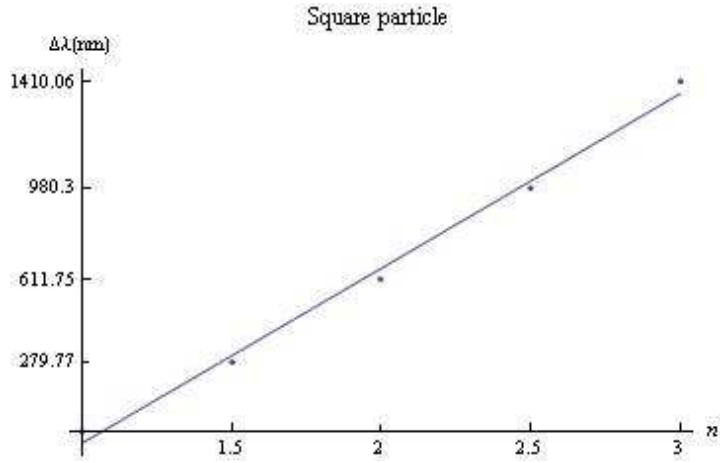

Figure 6. Squared split-ring: variation of the resonant wavelength as a function of the refractive index of the analyte.

ring and the omega particle behave reasonably well and with similar quality factor values. In the following section, we analyze also the sensitivity properties of the inclusions reported in Tables 3–4, in order to determine the optimal individual inclusion exhibiting the best combined selectivity and sensitivity performances.

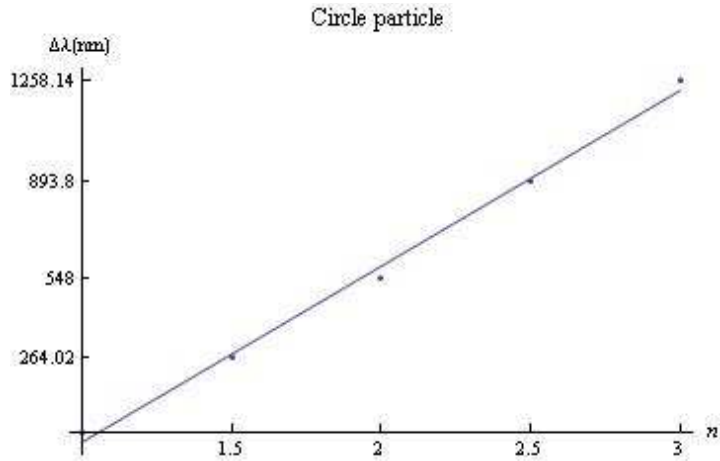

Figure 7. Circular split-ring: variation of the resonant wavelength as a function of the refractive index of the analyte.

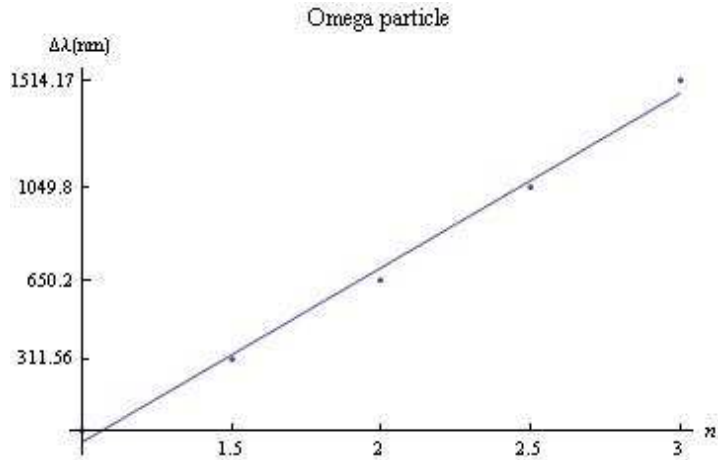

Figure 8. Omega particle: variation of the resonant wavelength as a function of the refractive index of the analyte.

6. SENSITIVITY ANALYSIS

Sensor sensitivity is expressed in terms of the output variation (i.e., the frequency shift Δf) corresponding to a unit change of the input (i.e., the unit variation of either permittivity ε or refractive index n). Therefore, sensor sensitivity S is given by $S = df/dn$. In first approximation, if the refractive index variation range is sufficiently narrow, the input-output relation can be considered as linear, as confirmed by the full-wave simulations run with CST Studio Suite [21].

On top of the array of inclusions a test material with thickness

Table 6. Comparison of the FOM values for different types of individual inclusions.

Single squared split-ring [22]	**2.08**		**Single rectangular split-ring [22]**	**0.39**
Coupled squared split-ring [22]	**1.51**		**Coupled rectangular split-ring [22]**	**0.19**
Coupled asymmetric split-ring [22]	**2.86**		**Squared split-ring (this paper)** 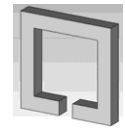	**8.22**
Circular split-ring (this paper)	**8.50**		**Omega particle (this paper)** 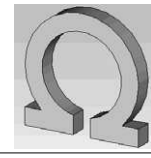	**8.48**

50 nm (as in [22]) with a varying refractive index n in the range 1–3 has been placed. In Figures 6–8, the obtained variations (performed by full-wave simulations) of the resonant wavelength as a function of the refraction index for different types of inclusions (squared split-ring, circular split-ring, and omega particle) are presented. These values were calculated by full-wave simulations.

The sensitivity of a sensor is commonly determined by a proper figure of merit (FOM) defined as [22]:

$$\mathrm{FOM} = \frac{m}{\mathrm{FWHM}} \tag{14}$$

where m is the slope of the curve $\Delta\lambda = f(n)$, expressed innm/RIU (Refractive Index Unit) and FWHM is the full width at half maximum expressed in nm. In Table 6, we report the values of the FOM for the individual inclusions studied in this paper and for other inclusion types already presented in the literature [22].

As evident from the table, the different types of the inclusions proposed in the paper give similar values of sensitivity. On the other side, it is confirmed that, as reported in Table 2, the collision frequency γ of the metallic material, the periodicity of the array Λ, and the permittivity/thickness of the adhesion layer play an important role on the sensitivity of the sensor, as they directly affect the FWHM. Once proper materials are chosen (in our case silver for the metallic parts and TiO_2 for the adhesion layer) sensor sensitivity can be adjusted by varying the lattice constant Λ of the array and the thickness of the adhesion layers. By optimizing such geometrical parameters, we have been able to achieve a higher sensitivity compared to the sensors already proposed in the literature and summarized by the results presented in [22] (Table 6).

7. CONCLUSIONS

In this paper, we have proposed the design of metamaterial-based biosensors consisting of planar arrays of metallic particles. Different shapes of the particles have been considered — namely squared split-ring, circular split-ring, and omega particle — showing for each of them the resulting selectivity and sensitivity performances. The final goal, in fact, has been to verify the ability of the proposed structures to be successfully used as biosensors working in the THz regime.

An analytical circuit model has been developed for each of the considered inclusions, in order to describe their resonant behavior. Particularly, compared to the models already presented in literature, we have added a new term for the fringing capacitances, incorporating the substrate effect, where the inclusions are deposited on, and the

adhesion layer presence. The proposed models have been successfully verified, by comparing the results to the ones obtained with full-wave numerical simulations.

Exploiting the proposed models, the effects of the variation of the geometrical and electrical parameters on the sensor selectivity and sensitivity have been reported and a proper comparison has been made between the three inclusion types considered in this paper and other setups already proposed in the literature. The extensive and comprehensive parametric analysis of the proposed structures allowed us to design biosensors with higher selectivity and sensitivity compared to the ones already presented in the open technical literature.

REFERENCES

1. Vo-Dinh, T. and L. Allain, "Biosensors for medical applications," *Biomedical Photonics Handbook*, CRC Press, 2003.
2. Hu, M., J. Chen, Z. Y. Li, L. Au, G. V. Hartland, X. Li, M. Marquez, and Y. Xia, "Gold nanostructures: Engineering their plasmonic properties for biomedical applications," *Chem. Soc. Rev.*, Vol. 35, 1084–1094, 2006.
3. Salamon, Z., H. A. Macleod, and G. Tollin, "Surface plasmon resonance spectroscopy as a tool for investigating the biochemical and biophysical properties of membrane protein systems. I. Theoretical principles," *Biochim. Biophys. Acta*, Vol. 1331, 117–129, 1997.
4. Lillie, J. J., M. A. Thomas, N. M. Jokerst, S. E. Ralph, K. A. Dennis, and C. L. Handerson, "Multimode interferometric sensors on silicon optimized for fully integrated complementary metal-oxide-semiconductor chemical-biological sensor systems," *J. Opt. Soc. Am. B*, Vol. 23, 642–651, 2006.
5. Luo, D. H., R. A. Levy, Y. F. Hor, J. F. Federici, and R. M. Pafchek, "An integrated photonic sensor for in situ monitoring of hazardous organics," *Sens. Actuators B*, Vol. 92, 121–126, 2003.
6. Xia, F., L. Sekaric, and Y. A. Vlasov, "Mode conversion losses in silicon-on-insulator photonic wire based racetrack resonators," *Opt. Expr.*, Vol. 14, 3872–3886, 2006.
7. Chao, C. Y. and L. J. Guo, "Biochemical sensors based on polymer microrings with sharp asymmetrical resonance," *Appl. Phys. Lett.*, Vol. 83, 1527–1529, 2003.

8. Yalçin, A., K. C. Popat, J. C. Aldridge, T. A. Desai, J. Hryniewicz, N. Chbouki, B. E. Little, O. King, V. Van, S. Chu, D. Gill, M. Anthes-Washburn, M. Selim Unlu, and B. B. Goldberg, "Optical sensing of biomelecules using microring resonators," *IEEE J. Selected Topics in Quantum Electronics*, Vol. 12, 148–155, 2006.
9. Wongkasem, N., A. Akyurtlu, J. Li, A. Tibolt, Z. Kang, and W. D. Goodhue, "Novel broadband terahertz negative refractive index metamaterials: Analysis and experiment," *Progress In Electromagnetics Research*, Vol. 64, 205–218, 2006.
10. Ishimaru, A., S. Jaruwatanadilok, and Y. Kuga, "Generalized surface plasmon resonance sensors using metamaterials and negative index materials," *Progress In Electromagnetics Research*, Vol. 51, 139–152, 2005.
11. Cai, M. and E. P. Li, "A novel terahertz sensing device comprising of a parabolic reflective surface and a bi-conical structure," *Progress In Electromagnetics Research*, Vol. 97, 61–73, 2009.
12. Bilotti, F., A. Toscano, L. Vegni, K. Aydin, K. B. Alici, and E. Ozbay, "Equivalent-circuit models for the design of metamaterials based on artificial magnetic inclusions," *IEEE Trans. Microw. Theory Tech.*, Vol. 55, 2865–2873, 2007.
13. Bilotti, F., A. Toscano, and L. Vegni, "Design of spiral and multiple split-ring resonators for the realization of miniaturized metamaterial samples," *IEEE Trans. Antennas Propag.*, Vol. 55, 2258–2267, 2007.
14. Tretyakov, S. A., "On geometrical scaling of split-ring and double-bar resonators at optical frequencies," *Metamaterials*, Vol. 1, 140–143, 2007.
15. Buoeno, M. A. and A. K. T. Assis, "A new method for inductance calculations," *J. Phys. D: Appl. Phys.*, Vol. 28, 1802–1806, 1995.
16. Delgado, V., O. Sydoruk, E. Tatartschuk, R. Marqués, M. J. Freire, and L. Jelinek, "Analytical circuit model for split ring resonators in the far infrared and optical frequency range," *Metamaterials*, Vol. 3, 57–62, 2009.
17. Pendry, J. B., A. J. Holden, D. J. Robbins, and W. J. Stewart, "Magnetism from conductors and enhanced nonlinear phenomena," *IEEE Trans. Microw. Theory Tech.*, Vol. 47, 2075–2081, 1999.
18. Tretyakov, S. A., F. Mariotte, C. R. Simovski, T. G. Kharina, and J. P. Heliot, "Analytical antenna model for chiral scatterers: Comparison with numerical and experimental data," *IEEE Trans. Antennas Propag.*, Vol. 44, 1006–1014, 1996.

19. Simovski, C. R., S. A. Tretyakov, A. A. Sochava, B. Sauviac, F. Mariotte, and T. G. Kharina, "Antenna model for conductive omega particles," *Journal of Electromagnetic Waves and Applications*, Vol. 11, No. 11, 1509–1530, 1997.
20. Casse, B. D. F., H. O. Moser, O. Wilhelmi, and B. T. Saw, "Micro- and nano-fabrication of electromagnetic metamaterials for the terahertz range," *Proceedings of the ICMAT 2005 Symposium*, 18–25, 2005.
21. CST Computer Simulation Technology, www.cst.com.
22. Chen, C.-Y., I.-W. Un, N.-H. Tai, and T.-J. Ye, "Asymmetric coupling between subradiant and superradiant plasmonic resonances and its enhanced sensing performance," *Opt. Expr.*, Vol. 17, 15372–15380, 2009.